Sub-Lithospheric Small-Scale Convection Tomographically Imaged Beneath the Pacific Plate

Zachary C Eilon[1], Lun Zhang[1], James B. Gaherty[2], Donald W. Forsyth[3], and Joshua B. Russell[3]

[1]University of California Santa Barbara
[2]Northern Arizona University
[3]Brown University

November 22, 2022

Abstract

Small-scale convection beneath the oceanic plates has been invoked to explain off-axis non-plume volcanism, departure from simple seafloor depth-age relationships, and intraplate gravity lineations. We deployed thirty broadband OBS stations on ˜40 Ma seafloor in the equatorial Pacific, in a region notable for gravity anomalies measured by satellite altimetry elongated in the direction of plate motion. P-wave teleseismic tomography reveals alternating upper mantle velocity anomalies on the order of ±2%, oriented parallel to the gravity lineations. These features, which correspond to ˜300-500 @K lateral temperature contrast, and possible hydrous or carbonatitic partial melt, are strongest between 150 and 260 km depth, indicating rapid vertical motions through a low-viscosity asthenospheric channel. Coherence and admittance analysis using new multibeam bathymetry soundings substantiates the presence of asthenospheric density variation, and forward modelling predicts gravity anomalies that qualitatively match observed lineations. This study provides observational support for small-scale convective rolls beneath the oceanic plates.

Posted on 22 Nov 2022 — CC-BY-NC 4 — https://doi.org/10.1002/essoar.10511983.1 — This a preprint and has not been peer reviewed. Data may be preliminary.

Sub-Lithospheric Small-Scale Convection Tomographically Imaged Beneath the Pacific Plate

Zachary C. Eilon[1], Lun Zhang[1], James B. Gaherty[2], Donald W. Forsyth[3], and Joshua B. Russell[3]

[1] University of California Santa Barbara, Santa Barbara, CA

[2] Northern Arizona University, Flagstaff, AZ

[3] Brown University, Providence, RI

Corresponding author: Zachary Eilon (eilon@ucsb.edu)

Key Points:

- A broadband OBS array in the equatorial Pacific allows P-wave imaging of the uppermost mantle in a region of elongated gravity anomalies
- We observe elongated P-wave velocity anomalies of order ±2% beneath the oceanic lithosphere, striking parallel to gravity lineations
- These anomalies are inferred to arise from small scale convective cells beneath the plate with planform parallel to absolute plate motion

Key words:
Oceanic lithosphere
Asthenosphere
Mantle convection
Body wave tomography
Ocean Bottom Seismometer

Abstract

Small-scale convection beneath the oceanic plates has been invoked to explain off-axis non-plume volcanism, departure from simple seafloor depth-age relationships, and intraplate gravity lineations. We deployed thirty broadband OBS stations on ~40 Ma seafloor in the equatorial Pacific, in a region notable for gravity anomalies measured by satellite altimetry elongated in the direction of plate motion. P-wave teleseismic tomography reveals alternating upper mantle velocity anomalies on the order of ±2%, oriented parallel to the gravity lineations. These features, which correspond to ~300-500 ˚K lateral temperature contrast, and possible hydrous or carbonatitic partial melt, are strongest between 150 and 260 km depth, indicating rapid vertical motions through a low-viscosity asthenospheric channel. Coherence and admittance analysis using new multibeam bathymetry soundings substantiates the presence of asthenospheric density variation, and forward modelling predicts gravity anomalies that qualitatively match observed lineations. This study provides observational support for small-scale convective rolls beneath the oceanic plates.

Plain Language Summary

Covered by kilometers of water, and therefore hard to access, Earth's oceanic tectonic plates have several features we cannot explain. Among these are linear undulations ("rolls") in the strength of gravity at the sea surface. Using data from a rare underwater seismic experiment, we have produced 3-D maps of seismic properties of Earth's sub-surface in a location of clear gravity rolls. We find linear blobs of fast and slow material in the mantle beneath the oceanic plate, parallel to the gravity features. These represent cold sinking and warmer rising material, revealing a highly dynamic convective system underneath the plate which has long been theorized but not previously directly observed at this scale.

1. Introduction

Traditional plate tectonic models fail to explain several aspects of the oceanic lithosphere. For instance, widespread off-axis, non-plume volcanism within the Pacific plate has unknown origin (Ballmer et al., 2009; D. T. Sandwell et al., 1995), while the depth-age relationship predicted by lithospheric conductive cooling models breaks down in old (>70 Ma) ocean plates with anomalously shallow seafloor topography and high heat flow (Crosby et al., 2006; Parsons & Sclater, 1977; Parsons & McKenzie, 1978; Stein & Stein, 1992). Sub-lithospheric small scale convection (SSC) (Ballmer et al., 2007; Buck, 1985; Haxby & Weissel, 1986) has been proposed to explain these phenomena. This dynamic process, which is favored by a thicker, lower-viscosity asthenospheric layer, would increase the heat flow at the base of the lithospheric thermal boundary layer, and could concentrate upwellings and consequent melting. SSC spontaneously develops in the upper mantle due to the instabilities at the base of lithosphere whenever its thickness exceeds a critical value (Ballmer et al., 2007; Buck & Parmentier, 1986). It is expected to take the form of convective rolls aligned with absolute plate motion (APM) (Buck & Parmentier, 1986; Richter & Parsons, 1975) (Fig. 1b) due to shear between the plate and the deeper mantle. Despite the geodynamic significance of SSC beneath the oceanic plates, it has never previously been directly imaged at length scales <~2000 km (French et al., 2013) with seismic tomography beneath mature oceanic plate.

To date, the most powerful argument for widespread SSC beneath the plates are free air gravity lineations observed in the oceans, aligned parallel to APM and with wavelength of ~150-400 km, comparable to SSC predictions (Haxby & Weissel, 1986). Others have proposed alternative explanations for these gravity anomalies, including mechanical modification of the lithosphere and viscous fingering (Bull et al., 1992; Cormier et al., 2011; Gans et al., 2003; Sandwell & Fialko, 2004; Sandwell et al., 1995). Lithospheric boudinage (non-linear lithospheric extension) or thermal contraction bending (Fig. 1b) can produce elongated topographic and gravity undulations. Associated cracking might provide conduits for upward percolation of preexisting asthenospheric melt to form volcanic ridges; in this case the drainage of melt might lead to shallow high-velocity anomalies beneath the ridges (Karato & Jung, 1998). Viscous fingering, caused by lateral intrusion of low-viscosity material within a thin asthenospheric channel (Fig. 1b) has also been proposed to explain spreading-aligned ridge-adjacent seamounts, gravity variation, and long-wavelength velocity anomalies beneath young seafloor (Holmes et al., 2007; Weeraratne et al., 2007). Our study area is in older seafloor in a region with no volcanic ridges or major seamounts. Notably, gravity lineations here obliquely cross fracture zones (that record fossilized relative plate motion), suggesting they are not inherited from the mid-ocean ridges.

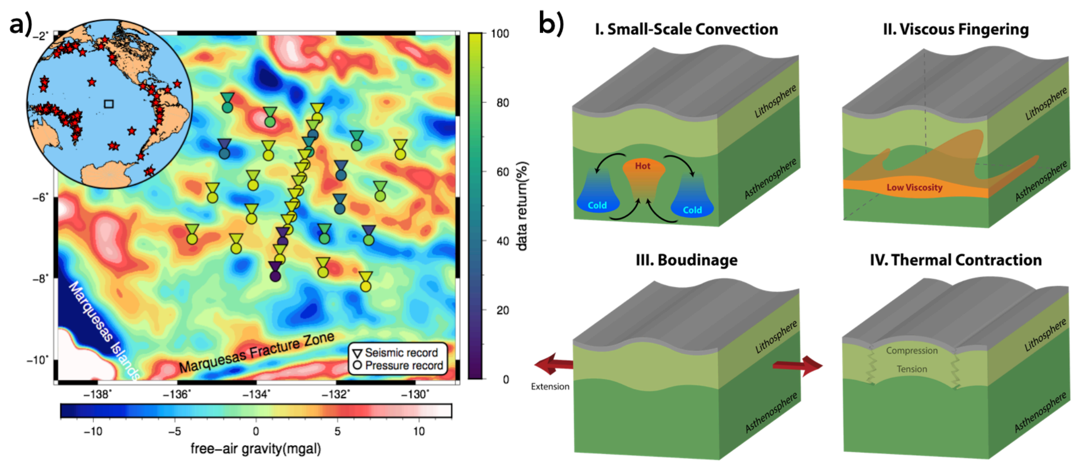

Fig. 1 | Map of the research area (a) and schematics of candidate processes causing gravity lineations (b). a*, Broadband OBS array comprising three-component seismometers (triangles) with differential pressure gauge (circles). Symbol colors indicate fractional data return, and the underlying map shows filtered free air gravity anomalies (Figure S9). Inset shows location of the array, with stars representing earthquakes from which differential travel times were measured.* ***b****, Block diagrams showing exaggerated lithospheric and asthenospheric structures proposed to explain free air gravity undulations (adapted after Weeraratne et al., 2007). Any bathymetric anomalies, exaggerated here, are highly contingent on elastic thickness of the lithosphere.*

Discriminating the above hypotheses requires tomographic resolution of features with <200 km lateral wavelength in the upper mantle, together with high-precision local constraints on bathymetry. Sparse island stations and ocean basin-traversing seismic rays offer only coarse imaging of the oceanic upper mantle. A previous study, the GLIMPSE Ocean Bottom Seismometer (OBS) experiment (Forsyth et al., 2006) aimed to probe gravity lineations in ~2-10 Ma Pacific plate just west of the East Pacific Rise (EPR). Body (Harmon et al., 2007) and Rayleigh wave (Weeraratne et al., 2007) imaging revealed elongate low velocity lineaments beneath volcanic ridges with lateral wavelength of order ~250 km. Substantial data loss precluded fine depth resolution with body waves, but velocity variation was estimated using surface waves to reside at <70 km depth. No other OBS experiments before or since have imaged uppermost mantle 3-D isotropic wave speed variations suggestive of small scale convection in regions unperturbed by plume or other intra- or inter-plate volcanic activity.

2. Data

The Pacific OBS Research into Convecting Asthenosphere (ORCA) experiment (Eilon et al., 2022) deployed 30 OBS instruments across a 500x500 km^2 footprint on ~40 Ma lithosphere northeast of Marquesas Islands. These instruments, deployed for 13 months, included three-component broadband seismometers and differential pressure gauges. The array was oriented approximately orthogonal to ±15 mGal free air gravity lineations observed from Seasat altimetry (Haxby & Weissel, 1986), with aperture spanning 2-3 wavelengths (~500 km) of the gravity rolls (Fig. 1a). This experiment also collected new high-resolution multibeam swath data which has been integrated into the global seafloor database (Smith & Sandwell, 1997) to provide substantially better constrained bathymetry in this region.

We extracted the vertical seismic and pressure waveforms for P-wave arrivals recorded on the ORCA array from teleseismic events (>30° distance; Fig. 1) in the GCMT catalogue between April 2018 and May 2019 with moment magnitudes ≥5.5. For each event, we measured relative arrival times of direct *P*-waves using multi-channel cross-correlation (MCCC; Fig. S1) (VanDecar & Crosson, 1990) on vertical and pressure records independently, yielding 1096 and 598 differential travel times respectively. We combined these data (see *Supporting Information*) to yield 1196 high-quality P-wave travel times (Supp. Fig. 2a).

3. Methods

We inverted these differential travel times for 3-D upper mantle *P*-wave velocity perturbations (δV_p) using a finite frequency tomography approach. To regularize the inverse problem we applied both model norm damping and first derivative damping (*i.e.*, "flattening") with a horizontal-to-vertical smoothing ratio of 2. We weighted observations by estimating travel time errors *a* *posteriori* during the MCCC process. To avoid unrealistically low estimated errors, we set a minimum standard deviation of 0.625s, equal to 1/20 of the central filter period. We solved for station and event static terms. Optimal regularization parameter values were determined by L-test. For a much more comprehensive description of the inverse problem, see the *Supporting Information*.

To explore apparent lineations in observed velocity structure, we conducted a series of "2.5-D" inversions by enforcing flattening (*i.e.*, no model variation) along a single horizontal direction, seeking a lineation direction that minimized data misfit. We also evaluated the resolution and reliability of our inversion through input-output tests that included checkerboard structures (Fig. S5) and velocity lineations that mimic features of dynamical interest (Fig. S4). For checkerboard tests, we quantify feature recovery using semblance (Zelt, 1998) computed at each point over a 3-D volume with radius equal to checker length scale. Finally, we performed a suite of inversions for which the model nodes below and above various "squeezing depths" were heavily damped. By evaluating the fractional reduction in overall data fit for each squeezed case, and observing whether or not the inversion re-injects structure once the damping is relaxed (see *Supporting Information*), we determined the depth range over which the data require major velocity anomalies.

4. Results

4.1 Tomographic inversion

Simple thermal cooling models predict essentially no upper mantle velocity heterogeneity on the length scale of this array. Nonetheless, we measured differential arrival times of up to ±0.5s (with an RMS of 0.27 s). This travel time variance substantially exceeds signal that can be produced in the crust, and systematic back azimuthal variations seen at several stations confirm this signal to have an upper mantle origin (Figure S2).

Our tomographic model shows substantial upper-mantle velocity structure. The most prominent pattern in the 3D model (Fig. 2) is alternating velocity anomaly bands parallel to local gravity lineations, with lateral wavelength ~250-300 km. The amplitude of these anomalies is on the order of ±2% (±2.3% for the 1-99 percentiles, or ±1.8% for the 2.5-97.5 percentiles, in the best resolved regions; Fig. S8). For our preferred model, the final RMS data error was 0.23s, the RMS of event static values was 0.10 s and the RMS of station static values was 0.01 s. The weighted variance reduction was 85.29%, indicating good data fit.

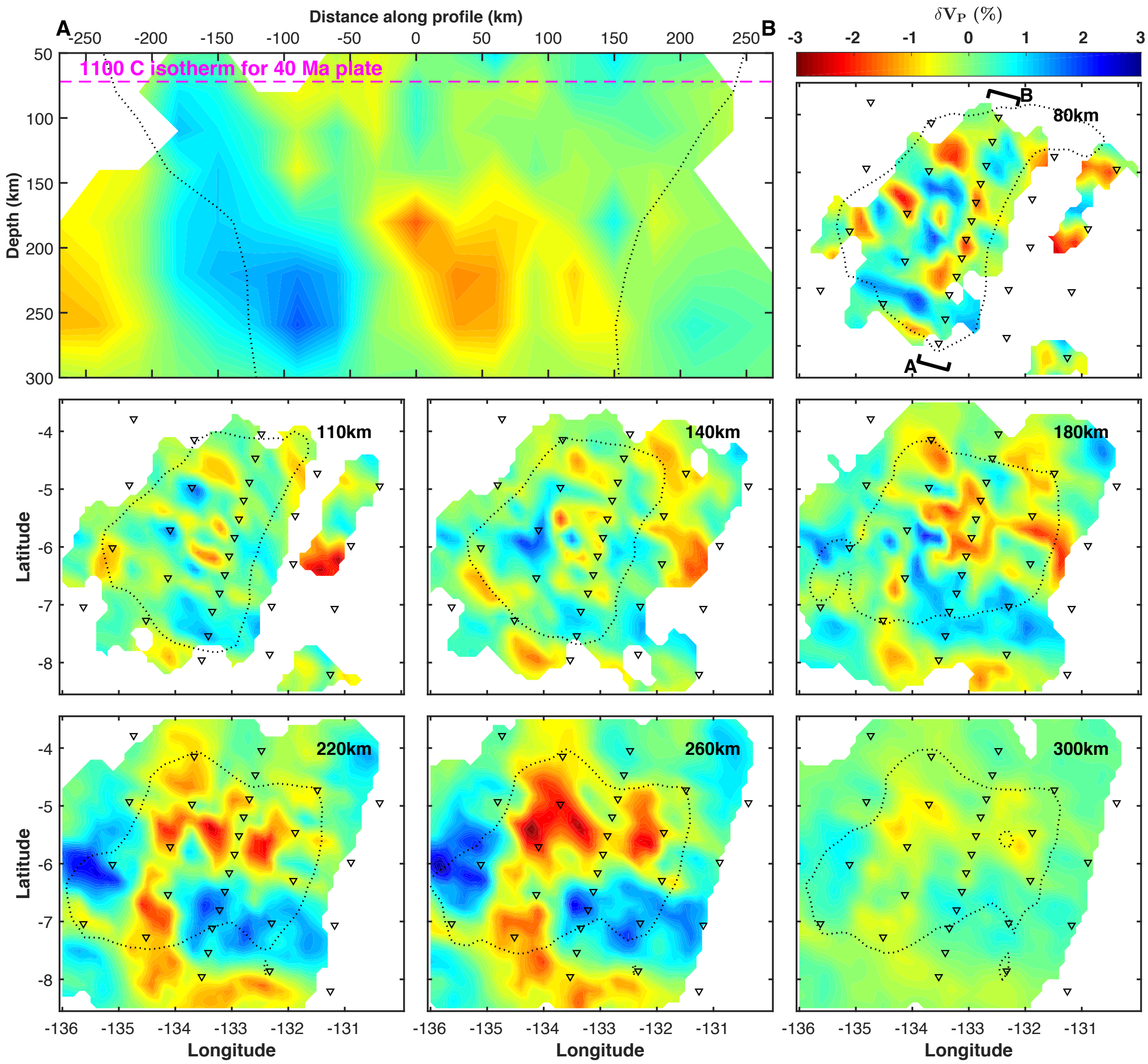

Fig. 2 | The tomographic model. *A vertical slice (top left) and several horizontal slices through our preferred 3-D δV_p model, where structure is shown only for model nodes with 'hit quality'* (Eilon et al., 2015) *above 0.3. Black dotted line shows region with semblance (a measure of checkerboard recovery* (Zelt, 1998)*) greater than 0.7. The vertical section depicts values averaged ±30 km in the direction perpendicular to the line of the section (indicated by black brackets in the 80 km depth cross-section), to avoid overly emphasizing any particular plane.*

4.2 Testing the model

2.5-D inversions to test for preferred lineation (Figs. 3, S7) showed that best fit to data (78% as good as the full 3-D model) involves structure elongated in the 115° direction (Fig. 3b). We infer that this direction reflects the dominant structural elongation. This orientation is subparallel to (independently constrained) gravity lineations and local absolute plate motion. Note, this minimum-misfit 2.5-D model (Fig. 3b) was used to compute 1-D gravity variations (Fig. 4).

Synthetic tests indicated that our data coverage can indeed recover the geometry and position of the observed features (Fig. 3, S4, S5). These tests – especially at the model edges – suffer from as much as 40% amplitude loss due to sparse seismic ray coverage. This observation, typical for these sorts of regularized inversions, theoretically implies that observed velocity, and hence inferred temperature, contrasts are in fact lower bounds.

We individually tested shallow squeezing and deep squeezing, finding that the data require relatively deep anomalies: at least 140km, and as much as 300 km in depth (Figs. S4, S6). We attempted to quantitatively determine the optimal depth range for the most prominent mantle velocity anomalies by squeezing structure into a moving window of three model layers (Fig. 3). These tests showed that the data require the most prominent anomalies to be fit by structure within the 180-260km depth range. This finding is not particular to a three-layer test; similar two- and four-layer tests confirmed that the 140-260 km depths are most important to fitting the data. This finding does not preclude structure at other depths in the model, rather it indicates that velocity anomalies in this depth range have the greatest influence on measured travel times. Lastly, we explored the depth extent of imaged features by increasing the model base to 480 km (Fig. S6). We found that although some structure is smeared to depths >300 km, the pattern of the anomalies is extremely similar to the preferred model, and the strongest anomalies are still present in the 150-300 km depth range.

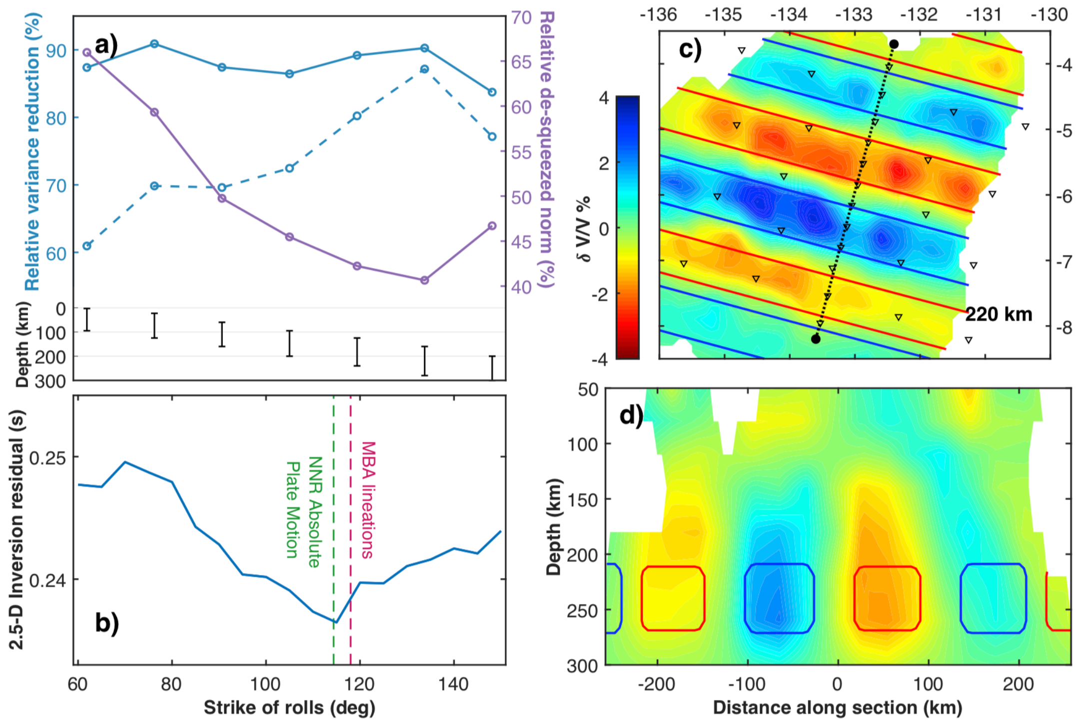

Fig. 3 | Tests of the tomographic model. a) *Squeezing tests of anomaly depth. Lower subplot shows depth extent over which structure was allowed to enter into the model space, while upper subplot shows data fit (measured by variance reduction – high values indicate better data fit) and explanatory power of the un-squeezed region of model space (purple line; low values indicate the squeezed model does a better job of explaining the data) for the associated models. Variance reduction is plotted relative to the un-damped, preferred, model. De-squeezed model norm is plotted relative to the norm of the squeezed model in each iteration and can thus be thought of as fractional model addition once squeezing is relaxed.* ***b)*** *Tests of feature elongation direction, showing data misfit (residual) when grid searching through possible orientations of 2.5-D models.* ***c)*** *Horizontal slice and* ***d)*** *vertical section through models yielded by synthetic recovery tests with input rectangular velocity anomalies (dashed lines) of ±4%.*

4.3 Gravity signals

The ORCA experiment measured high-resolution multibeam topography throughout the OBS array footprint, allowing for detailed comparison with gravity (Fig. S9). To identify subsurface density heterogeneity, we computed free air coherence and admittance, and the theoretical mantle Bouguer anomaly (MBA; see *Supporting Information*). At wavelengths greater than 20 km, observed free air admittance in this region is approximately 0.025 mGal/m. This value is substantially less than the theoretical admittance for uncompensated topography, but also significantly greater than the prediction for topography compensated at the Moho (Fig. S10).

5. Discussion and conclusions

5.1 Thermal anomalies

The tomographic models show alternating slow and fast δV_p features within the oceanic asthenosphere. We infer that these features result from hot upwellings and cold downwellings, respectively. These cells take the approximate form of cylindrical rolls, with horizontal length scale ~250-300 km and aspect ratio approximately unity. These features are not consistent with lithospheric warping (boudinage or cracking), which predict negligible, and certainly not >200 km deep, upper-mantle velocity variations. They are also not consistent with viscous fingering, which would require velocity variations confined to a shallow (<100 km deep) and thin (<30 km thick) channel (Weeraratne & Parmentier, pers. comm.) Rather, these observations provide the first tomographic evidence for small-length-scale thermal convection beneath the oceanic plates, aligned by shear between the plate and underlying deeper mantle.

Differential travel time tomography provides constraints only on lateral velocity gradients, not absolute velocity. The ~4% peak-to-peak amplitude of the observed velocity anomalies is relatively high. Absent melt, this implies up to ~ 500˚C lateral temperature variations (see *Supporting Information*; Fig. S8). Our default expectation is that SSC is driven here by positive density anomalies that drip or sink from the base of the lithospheric thermal boundary layer. In this framework, the fast *dVp* anomalies correspond to material that is cold in an absolute sense, while the slow *dVp* anomalies represent relatively warm ambient mantle.

However, upwelling parcels displaced by the downwellings must undergo adiabatic decompression. If the mantle contains dissolved volatiles, this upwelling material could produce small-fraction hydrous and/or carbonatitic melt fraction even at depths up to 200 km (Dasgupta et al., 2013; Hirschmann, 2010). Melting could introduce a small active component to upwellings by reducing density and viscosity. Melt would also lower the absolute P-wave velocity in the upwelling cells. Accounting for both elastic and anelastic effects (see *Supporting Information*), the observed peak-to-peak dVp variation can also be explained by a 0.5% melt fraction, together with a dT of ~ 300°C (Fig. S8). We prefer this latter (temperature plus melt) scenario for explaining observed anomalies, since the implied temperature gradient is more consistent with (although still greater than) the temperature contrast invoked in numerical models of sub-lithospheric SSC (Ballmer et al., 2009; Manjón-Cabeza Córdoba & Ballmer, 2021). This same analysis predicts a Q_μ of 100-180 in the oceanic asthenosphere, consistent with previous observations (Ma et al., 2020).

5.2 Gravity analysis and modelling

A closer examination of observed gravity anomalies provides further insight. Free air admittance indicates some degree of isostatic compensation here. Remaining support for bathymetry must come from plate strength, in line with previous >15 km estimates of effective elastic thickness here (Fischer et al., 1986).

The observed compensation must result from some combination of crustal thickness variations and upper mantle density anomalies. Three primary observations suggest a substantial influence from the upper mantle. Firstly, MBA anomalies here (striking ~120°) are oriented sub-parallel to plate motion (~115°), rather than the paleo-spreading direction inferred from abyssal hill fabric and nearby fracture zones (~75°, although we do note a due E-W swath of seafloor in this region with ~105° apparent spreading direction indicated by the trend of the abyssal hill topography (Eilon et al., 2022), perhaps due to oblique spreading, a ridge jump or large overlapping spreading center). Secondly, if the observed gravity and bathymetry anomalies were created from a single mechanism then the coherence should be unity. We observe coherence lower than 0.7 associated with the longest-wavelengths (Fig. S10). Finally, the predicted free air anomaly for compensation at Moho depths under-predicts the admittance, requiring either deeper compensation or density anomalies beneath an elastic plate with flexural rigidity that dampens the topographic expression. Our inference is that multiple mechanisms are at play here, pointing to the loading of a finite-rigidity plate from below as a result of density variations in the mantle, in addition to “frozen-in” partial compensation of the topographic relief by variations in crustal thickness.

As a proof-of-concept, we explored the correspondence between the MBA and our velocity model. For simplicity, and given the strongly linear features in both models, we collapsed the MBA to 1.5 dimensions (*i.e.*, varying in the roll-perpendicular-direction but homogenous in the roll-parallel-direction), using a log-spaced sinusoidal basis. The best fit 1.5-D gravity field (explaining 28% of the full 2-D signal) comprises lineations aligned 118˚ from North. We compare this gravity anomaly to the 2.5-D velocity model smoothed in the same direction, considering dV_P variations only in the plane defined by the vertical and the direction perpendicular to the gravity rolls (Fig. 4). There is no direct association between the pattern of deep (200-300 km) dV_P anomalies and the residual gravity, other than similarity in their wavelength (225-300 km) of variation and orientation of the lineations. This is not surprising: periodic density anomalies at depth approximately equal to their wavelength should negligibly affect surface gravity due to upward continuation. However, using our 2.5-D tomography model to forward calculate 1.5-D gravity variations (see *Supporting Information*, and note this calculation used the more modest temperature variation outlined above, adding support to that scenario), we found good qualitative match between observed and predicted signal, where the predicted signal is dominated by the shallowest features in the velocity model (Fig. 4). Although this portion of the model is not as well resolved, the agreement is striking and demonstrates that mantle temperature heterogeneity alone can theoretically explain the MBA gravity anomaly.

5.3 Asthenospheric rheology

The depth, vertical extent, and wavelength of putative convective features imaged in this study connect to the rheology of the asthenosphere. The presumed source of convective instability, is near the base of the plate. For 40 Ma oceans (assuming mantle potential temperature, T_m, of 1350˚C and thermal diffusivity of 10^{-6} m^2/s), the depth to the 1150˚C isotherm (the 0.85 $T_m$value often used to approximate the thermal lithosphere-asthenosphere boundary) is 73 km. The agreement between the strike of the rolls and local APM in a no-net rotation reference frame (DeMets et al., 2010), together with the lack of another obvious alternative source for small-scale lateral thermal gradients, argues that these features are not deep-rooted but derive from convective processes near the bottom of the plate. Station spacing limits our resolution shallower than ~50 km, but synthetic recovery tests indicate that we should have imaged large-scale velocity anomalies in the 100-200 km depth range, if they were present (Figs. S4, S5). It is surprising, then, that the strongest velocity features in the model are as deep as 250 km and that squeezing tests suggest that the strongest anomalies are deeper than 200 km (Fig. 3).

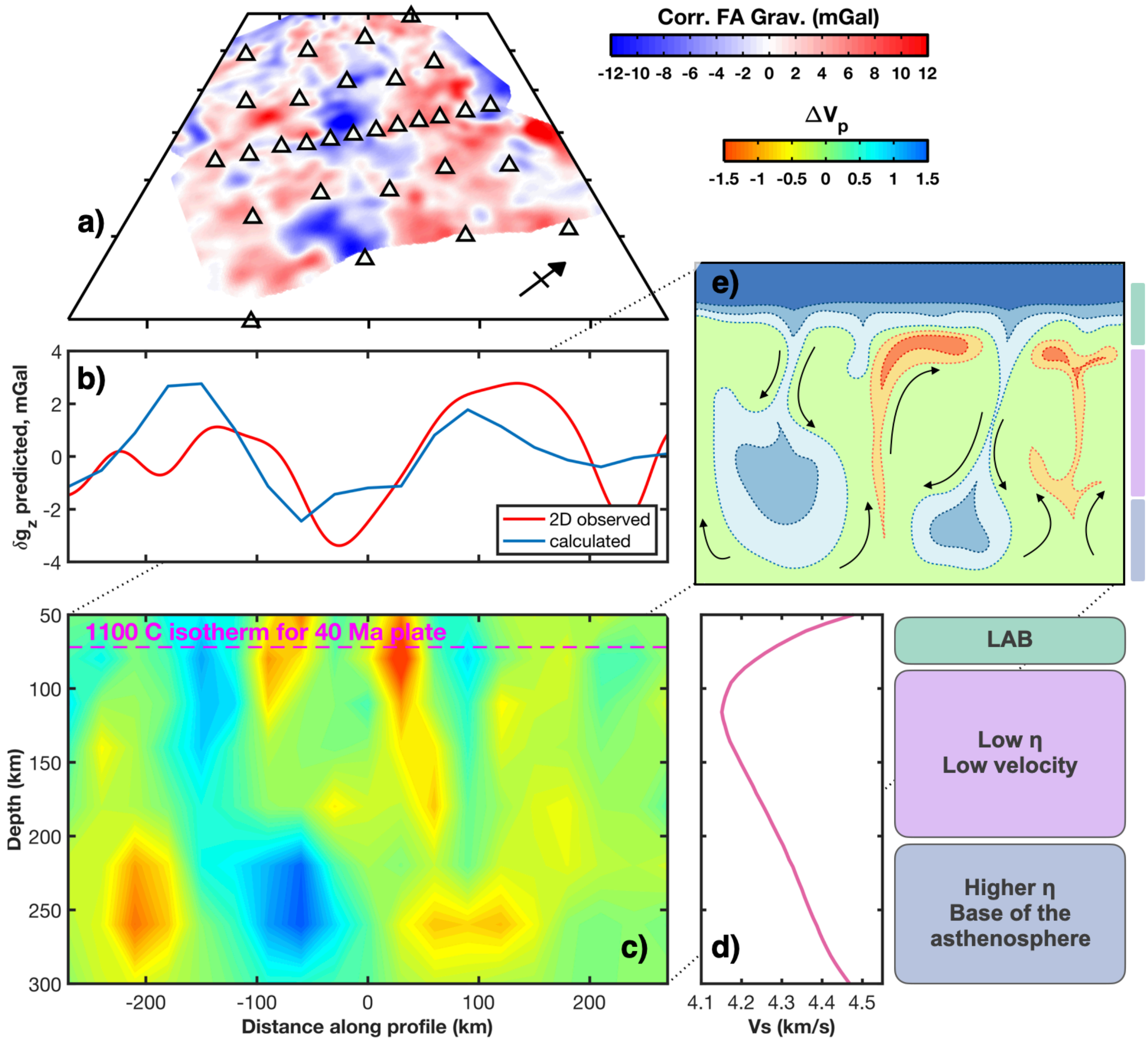

Fig. 4 | Dynamic summary and comparison between gravity and tomography. a) *Mantle Bouguer gravity anomaly corrected for effects of bathymetry and filtered as in Fig. S9.* ***b)*** *One-dimensional variation in gravity anomaly obtained from sinusoidal fitting of observed field (red) and velocity-temperature-density forward modelling (blue) of the model depicted in panel (c). The orientation of the section is ~30° east of North.* ***c)*** *Cross section through the 2.5-D velocity model,* *perpendicular to enforced smoothing direction.* ***d)*** *1-D shear velocity profile obtained from inversion of Rayleigh wave phase velocities averaged across ORCA array* (Russell, 2021). ***e)*** *Cartoon cross-section of small scale convection beneath the plate, where bluer colors correspond to colder and more dense material and redder colors correspond to hotter and less dense material.*

A comparison between Rayleigh wave imaging at young ORCA and NoMelt (70 Ma crust) indicates that the young ORCA region exhibits anomalously slow absolute shear velocity beneath the plate (Fig. 4), with a broad velocity minimum from 75-200 km depth (Russell et al., 2021). Small scale convection is favored by a wider low viscosity layer, and the middle of this layer is expected to be roughly isothermal. Our observed anomalies appear deeper than the slowest (and presumably weakest) part of the asthenosphere. It is possible that density anomalies are preserved at lithospheric levels (<100 km depth) and deeper than 200 km due to higher viscosity, while the lowest-viscosity portion of the asthenosphere is roughly isothermal and contains convective structures too fine to resolve. A similar mechanism has been suggested to explain a minimum in the strength of azimuthal anisotropy in the center of the oceanic asthenosphere observed by other focused OBS arrays (Lin et al., 2016; Russell et al., 2019).

This suite of observations suggests a sub-lithospheric SSC system wherein the gravity and velocity anomalies correspond to the upper and lower thermal boundary layers of an asthenosphere-scale convective system, respectively. We posit three depth regimes (Fig 4): 1) The base of the plate (50-100 km), the source of the density instabilities and part of the Bouguer gravity anomalies. The elastic lithosphere partially damps the effect on bathymetry. 2) The low-viscosity center of the asthenosphere (100-200 km), coinciding with the lowest velocities in a surface-wave-derived 1-D shear velocity model (Fig. 4). Imaged anomalies in this regime are minimal, despite good resolving power. We infer that once an instability develops, it sinks rapidly through the low viscosity asthenosphere (Ballmer et al., 2009), perhaps leaving behind thin convective sheets or spokes connecting regimes (1) and (3) that are too narrow to be imaged tomographically. 3) A higher viscosity base of the asthenosphere (200-300 km), where high-density anomalies encounter resistance to sinking and pile up, making for clearly imaged velocity anomalies. Ambient mantle displaced upwards at this depth begins to melt (requiring volatiles to reduce the solidus (Dasgupta et al., 2013; Hirschmann, 2010)), reducing seismic velocities in the upwelling volumes between the downwelling limbs.

This work provides evidence for a highly dynamic asthenospheric system beneath the central oceanic plates, involving small scale lithospheric delamination, and small-fraction hydrous and/or carbonatite melt. Since intraplate volcanism is not ubiquitous in the oceans, upward pathways for melt transport through the lithosphere must be rare. Rather, this melt may pond or freeze in laminae at the base of the plate, contributing to a sharp and possibly radially anisotropic LAB structure observed widely in the Pacific (Beghein et al., 2014; Kawakatsu et al., 2009; Stern et al., 2015). In addition, SSC might introduce uneven topography on the LAB that is not a simple function of age. Together, these phenomena help explain the variability in seismic discontinuities in the uppermost (<100 km depth) oceanic mantle (Schmerr, 2012; Tharimena et al., 2017).

Acknowledgments

This work was funded by NSF grants OCE-1658491, OCE-1658214, OCE-1658070, and OCE-2051265. The OBS instruments were provided by the Scripps Institution of Oceanography, coordinated by the OBS Instrument Centre at the Woods Hole Oceanographic Institute. We are grateful to Dave Sandwell for sharing codes and illuminating discussions. We thank the ships' captains, crew, and research technicians, as well as the cruise science parties, who were all indispensable to collecting these data. The authors declare no conflicts of interest associated with this study.

Open Research: Data and code availability

The seismic data from this experiment are available through the Incorporated Research Institutions for Seismology's Data Management Center, under the network code XE (2018-2019). Metadata information is catalogued within Eilon et al. (2022) (DOI 10.1785/0220210173). Multibeam swath bathymetry data is available via the Rolling Deck to Repository portal (DOIs 10.7284/907958 and 10.7284/908257). Free air gravity data is available at https://topex.ucsd.edu/pub/global_grav_1min/ and bathymetry at https://topex.ucsd.edu/pub/global_topo_1min. Codes for all the analysis and figures above are provided via a Dryad repository [#DOI insert available after submission#].

References

Abers, G. A., & Hacker, B. R. (2016). A MATLAB toolbox and Excel workbook for calculating the densities, seismic wave speeds, and major element composition of minerals and rocks at pressure and temperature. *Geochemistry Geophysics Geosystems*, *17*(2), 616–624. https://doi.org/10.1002/2015gc006171

Ballmer, M. D., Hunen, J. van, & Ito, G. (2007). Non-hotspot volcano chains originating from small-scale sublithospheric convection. *Geophysical Research Letters*, *34*, L23310. https://doi.org/10.1029/2007gl031636/pdf

Ballmer, M. D., Hunen, J. van, Ito, G., Bianco, T. A., & Tackley, P. J. (2009). Intraplate volcanism with complex age-distance patterns: A case for small-scale sublithospheric convection. *Geochemistry Geophysics Geosystems*, *10*(6), n/a-n/a.

Bechtel, T. D., Forsyth, D. W., & Swain, C. J. (1987). Mechanisms of isostatic compensation in the vicinity of the East African Rift, Kenya. *Geophysical Journal International*, *90*(2), 445–465. https://doi.org/10.1111/j.1365-246X.1987.tb00734.x

Beghein, C., Yuan, K., Schmerr, N., & Xing, Z. (2014). Changes in Seismic Anisotropy Shed Light on the Nature of the Gutenberg Discontinuity. *Science*, *343*(6176), 1237–1240. https://doi.org/10.1126/science.1246724

Behn, M. D., Hirth, G., & II, J. R. E. (2009). Implications of grain size evolution on the seismic structure of the oceanic upper mantle. *Earth and Planetary Science Letters*, *282*(1–4), 178–189. https://doi.org/10.1016/j.epsl.2009.03.014

Brunsvik, B. R., Eilon, Z. C., & Lynner, C. (2021). Mantle Structure and Flow Across the Continent-Ocean Transition of the Eastern North American Margin: Anisotropic *S* -Wave

Tomography. *Geochemistry, Geophysics, Geosystems*, *22*(12). https://doi.org/10.1029/2021GC010084

Buck, W. R. (1985). When does small-scale convection begin beneath oceanic lithosphere? *Nature*, *313*(6005), 775–777. https://doi.org/10.1038/313775a0

Buck, W. R., & Parmentier, E. M. (1986). Convection beneath young oceanic lithosphere: Implications for thermal structure and gravity. *Journal of Geophysical Research-Solid Earth and Planets*, *91*(B2), 1961–1974. https://doi.org/10.1029/jb091ib02p01961

Bull, J. M., Martinod, J., & Davy, P. (1992). Buckling of the oceanic lithosphere from geophysical data and experiments. *Tectonics*, *11*(3), 537–548. https://doi.org/10.1029/91TC02908

Cormier, M.-H., Gans, K. D., & Wilson, D. S. (2011). Gravity lineaments of the Cocos Plate: Evidence for a thermal contraction crack origin. *Geochemistry Geophysics Geosystems*, *12*(7), n/a-n/a. https://doi.org/10.1029/2011gc003573

Crosby, A. G., McKenzie, D., & Sclater, J. G. (2006). The relationship between depth, age and gravity in the oceans. *Geophysical Journal International*, *166*(2), 553–573. https://doi.org/10.1111/j.1365-246x.2006.03015.x

Dasgupta, R., Mallik, A., Tsuno, K., Withers, A. C., & Hirth, G. (2013). Carbon-dioxide-rich silicate melt in the Earth's upper mantle. *Nature*, *493*(7431), 211–215. https://doi.org/10.1038/nature11731

DeMets, C., Gordon, R. G., & Argus, D. F. (2010). Geologically current plate motions. *Geophysical Journal*, *181*, 1–80.

Eilon, Z., Abers, G. A., Gaherty, J. B., & Jin, G. (2015). Imaging continental breakup using teleseismic body waves: The Woodlark Rift, Papua New Guinea. *Geochemistry, Geophysics, Geosystems*, *16*(8), 2529–2548. https://doi.org/10.1002/2015GC005835

Eilon, Z. C., & Abers, G. A. (2017). High seismic attenuation at a mid-ocean ridge reveals the distribution of deep melt. *Science Advances*, *3*(5), e1602829. https://doi.org/10.1126/sciadv.1602829

Eilon, Z. C., Gaherty, J. B., Zhang, L., Russell, J., McPeak, S., Phillips, J., et al. (2022). The Pacific OBS Research into Convecting Asthenosphere (ORCA) Experiment. *Seismological Research Letters*, *93*(1), 477–493. https://doi.org/10.1785/0220210173

Fischer, K. M., McNutt, M. K., & Shure, L. (1986). Thermal and mechanical constraints on the lithosphere beneath the Marquesas swell. *Nature*, *322*(6081), 733–736. https://doi.org/10.1038/322733a0

Forsyth, D. W., Harmon, N., Scheirer, D. S., & Duncan, R. A. (2006). Distribution of recent volcanism and the morphology of seamounts and ridges in the GLIMPSE study area: Implications for the lithospheric cracking hypothesis for the origin of intraplate, non-hot spot volcanic chains. *Journal of Geophysical Research*, *111*(B11), n/a-n/a. https://doi.org/10.1029/2005jb004075

French, S., Lekic, V., & Romanowicz, B. (2013). Waveform tomography reveals channeled flow at the base of the oceanic asthenosphere. *Science*, *342*(6155), 224–227. https://doi.org/10.1126/science.1242248

Gans, K. D., Wilson, D. S., & Macdonald, K. C. (2003). Pacific Plate gravity lineaments: Diffuse extension or thermal contraction? *Geochemistry, Geophysics, Geosystems*, *4*(9), 1074. https://doi.org/10.1029/2002GC000465

Garcia, E. S., Sandwell, D. T., & Smith, W. H. F. (2014). Retracking CryoSat-2, Envisat and Jason-1 radar altimetry waveforms for improved gravity field recovery. *Geophysical Journal International*, *196*(3), 1402–1422. https://doi.org/10.1093/gji/ggt469

Hammond, W. C., & Humphreys, E. D. (2000). Upper mantle seismic wave velocity: Effects of realistic partial melt geometries. *Journal of Geophysical Research*, *105*(B5), 10975–10986. https://doi.org/10.1029/2000jb900041

Harmon, N., Forsyth, D. W., Lamm, R., & Webb, S. C. (2007). Pand Swave delays beneath intraplate volcanic ridges and gravity lineations near the East Pacific Rise. *Journal of Geophysical Research-Solid Earth and Planets*, *112*(B3), 1961–12. https://doi.org/10.1029/2006jb004392

Haxby, W. F., & Weissel, J. K. (1986). Evidence for small-scale mantle convection from Seasat altimeter data. *Journal of Geophysical Research*, *91*(B3), 3507–3520. https://doi.org/10.1029/jb091ib03p03507

Hirschmann, M. M. (2010). Partial melt in the oceanic low velocity zone. *Physics Of The Earth And Planetary Interiors*, *179*(1–2), 60–71. https://doi.org/10.1016/j.pepi.2009.12.003

Holmes, R. C., Webb, S. C., & Forsyth, D. W. (2007). Crustal structure beneath the gravity lineations in the Gravity Lineations, Intraplate Melting, Petrologic and Seismic Expedition (GLIMPSE) study area from seismic refraction data. *Journal of Geophysical Research*, *112*(B7), B07316. https://doi.org/10.1029/2006JB004685

Holtzman, B. K. (2016). Questions on the existence, persistence, and mechanical effects of a very small melt fraction in the asthenosphere. *Geochemistry Geophysics Geosystems*, *17*, 470–484. https://doi.org/10.1002/2015gc006102/pdf

Incorporated Research Institutions for Seismology. (2015). Data Services Products: Syngine. https://doi.org/10.17611/DP/SYNGINE.1

Jackson, I., & Faul, U. H. (2010). Grainsize-sensitive viscoelastic relaxation in olivine: Towards a robust laboratory-based model for seismological application. *Physics Of The Earth And Planetary Interiors*, *183*(1–2), 151–163. https://doi.org/10.1016/j.pepi.2010.09.005

Karato, S., & Jung, H. (1998). Water, partial melting and the origin of the seismic low velocity and high attenuation zone in the upper mantle. *Earth and Planetary Science Letters*, *157*(3–4), 193–207.

Kawakatsu, H., Kumar, P., Takei, Y., Shinohara, M., Kanazawa, T., Araki, E., & Suyehiro, K. (2009). Seismic evidence for sharp lithosphere-asthenosphere boundaries of oceanic plates. *Science*, *324*(5926), 499–502. https://doi.org/10.1126/science.1169499

Kennet, B., & Engdahl, E. R. (1991). Traveltimes for global earthquake location and phase identification. *Geophysics Journal International*, *105*, 429–465.

Lin, P., Gaherty, J. B., Jin, G., Collins, J. A., & Lizarralde, D. (2016). High-resolution seismic constraints on flow dynamics in the oceanic asthenosphere. *Nature*, *535*, 438–541.

Ma, Z., Dalton, C. A., Russell, J. B., Gaherty, J. B., Hirth, G., & Forsyth, D. W. (2020). Shear attenuation and anelastic mechanisms in the central Pacific upper mantle. *Earth and Planetary Science Letters*, *536*, 116148. https://doi.org/10.1016/j.epsl.2020.116148

Manjón-Cabeza Córdoba, A., & Ballmer, M. D. (2021). The role of edge-driven convection in the generation of volcanism – Part 1: A 2D systematic study. *Solid Earth*, *12*(3), 613–632. https://doi.org/10.5194/se-12-613-2021

Parsons, B, & Sclater, J. G. (1977). An analysis of the variation of ocean floor bathymetry and heat flow with age. *Journal of Geophysical Research*, *82*(5). Retrieved from http://www.agu.org/pubs/crossref/1977/JB082i005p00803.shtml

Parsons, Barry, & McKenzie, D. (1978). Mantle convection and the thermal structure of the plates. *Journal of Geophysical Research*, *83*(B9), 4485. https://doi.org/10.1029/JB083iB09p04485

Richter, F. M., & Parsons, B. (1975). On the interaction of two scales of convection in the mantle. *Journal of Geophysical Research*. https://doi.org/10.1029/jb080i017p02529/pdf

Russell, J., Gaherty, J. B., Eilon, Z. C., Forsyth, D. W., & Ekström, G. (2021). Heterogeneous Mantle Flow and Deviations fromm Half-Space Cooling Observed Beneath the Central Pacific. Presented at the AGU Fall Meeting 2021, New Orleans, LA, USA, DI15C-0033.

Russell, J. B. (2021). *Structure and Evolution of the Oceanic Lithosphere-Asthenosphere System from High-Resolution Surface-Wave Imaging* (PhD Thesis). *ProQuest Dissertations and Theses*. Retrieved from https://www.proquest.com/dissertations-theses/structure-evolution-oceanic-lithosphere/docview/2492599842/se-2?accountid=14522

Russell, J. B., Gaherty, J. B., Lin, P.-Y. P., Lizarralde, D., Collins, J. A., Hirth, G., & Evans, R. L. (2019). High-Resolution Constraints on Pacific Upper Mantle Petrofabric Inferred From Surface-Wave Anisotropy. *Journal of Geophysical Research*, *35*(3), 415–27. https://doi.org/10.1029/2018jb016598

Sandwell, D., & Fialko, Y. (2004). Warping and cracking of the Pacific plate by thermal contraction. *Journal of Geophysical Research*, *109*(B10). https://doi.org/10.1029/2004jb003091

Sandwell, D. T., Winterer, E. L., Mammerickx, J., Duncan, R. A., Lynch, M. A., Levitt, D. A., & Johnson, C. L. (1995). Evidence for diffuse extension of the Pacific Plate from Pukapuka ridges and cross-grain gravity lineations. *Journal of Geophysical Research: Solid Earth*, *100*(B8), 15087–15099. https://doi.org/10.1029/95JB00156

Schmandt, B., & Humphreys, E. (2010). Seismic heterogeneity and small-scale convection in the southern California upper mantle. *Geochemistry Geophysics Geosystems*, *11*(5), Q05004. https://doi.org/10.1029/2010gc003042

Schmerr, N. (2012). The gutenberg discontinuity: Melt at the lithosphere-asthenosphere boundary. *Science*, *335*(6075), 1480–1483. https://doi.org/10.1126/science.1215433

Smith, W. H. F., & Sandwell, D. T. (1997). Global Sea Floor Topography from Satellite Altimetry and Ship Depth Soundings. *Science*, *277*(5334), 1956–1962. https://doi.org/10.1126/science.277.5334.1956

Stein, C. A., & Stein, S. (1992). A model for the global variation in oceanic depth and heat flow with lithospheric age. *Nature*, *359*(6391), 123–129. https://doi.org/10.1038/359123a0

Stern, T. A., Henrys, S. A., Okaya, D., Louie, J. N., Savage, M. K., Lamb, S., et al. (2015). A seismic reflection image for the base of a tectonic plate. *Nature*, *518*(7537), 85–88. https://doi.org/10.1038/nature14146

Takei, Y., & Holtzman, B. K. (2009). Viscous constitutive relations of solid-liquid composites in terms of grain boundary contiguity: 1. Grain boundary diffusion control model. *Journal of Geophysical Research-Solid Earth and Planets*, *114*(B6), B06205. https://doi.org/10.1029/2008jb005850

Tharimena, S., Rychert, C., Harmon, N., & White, P. (2017). Imaging Pacific lithosphere seismic discontinuities—Insights from SS precursor modeling. *Journal of Geophysical Research: Solid Earth*, *122*(3), 2131–2152. https://doi.org/10.1002/2016JB013526

VanDecar, J. C., & Crosson, R. S. (1990). Determination of teleseismic relative phase arrival times using multi-channel cross-correlation and least squares. *Bulletin of the Seismological Society of America*, *80*(1), 150–169.

Weeraratne, D. S., Forsyth, D. W., Yang, Y., & Webb, S. C. (2007). Rayleigh wave tomography beneath intraplate volcanic ridges in the South Pacific. *Journal of Geophysical Research-Solid Earth and Planets*, *112*(B6), B06303. https://doi.org/10.1029/2006jb004403

Yamauchi, H., & Takei, Y. (2020). Application of a Premelting Model to the Lithosphere-Asthenosphere Boundary. *Geochemistry, Geophysics, Geosystems*, *21*(11). https://doi.org/10.1029/2020GC009338

Zelt, C. A. (1998). Lateral velocity resolution from three-dimensional seismic refraction data. *Geophysical Journal International*, *135*(3), 1101–1112.

AGU PUBLICATIONS

Geophysical Research Letters

Supporting Information for

Sub-lithospheric small-scale convection tomographically imaged beneath the Pacific plate

Zachary C. Eilon[1], Lun Zhang[1], James B. Gaherty[2], Donald W. Forsyth[3], and Joshua B. Russell[3]

[1] University of California Santa Barbara, Santa Barbara, CA
[2] Northern Arizona University, Flagstaff, AZ
[3] Brown University, Providence, RI
Corresponding author: Zachary Eilon (eilon@ucsb.edu)

Contents of this file

- Text S1
- Figures S1 to S10

Introduction

This supporting information includes additional information about methods useful for reproducing (but not essential for interpreting) the main article. Specifically, it includes:

- Details of the approach and parameters used for body wave differential travel time measurements
- A discussion of combining vertical and pressure channel measurements
- The tomographic model setup, parameter space, and inverse problem details
- The framework for determining regularization parameters for the inversion
- Details (in addition to those within the main text) of various tests of the model output and the data requirements of the model space
- A description of how we translated between velocity and temperature through forward calculations that rely on (an)elastic constitutive relationships.
- Math behind our calculation of gravity-topography admittance and coherence, including error analysis
- Math behind our calculation of 1.5D gravity anomalies from a 2.5D velocity model.

This file also contains 10 figures which assist the reader in interpretation of our results, and which contain additional tests to allow the reader to make their own judgments about our models.

Text S1

Body wave travel time measurements:

For each event, we measured relative arrival times of direct *P*-waves using multi-channel cross-correlation (MCCC; Fig. S1) (VanDecar & Crosson, 1990). This method uses a least-square inversion scheme to compute relative arrival times from cross-correlation pairs, reducing multi-path effects as well as the strict requirement for waveform similarity. As a default, we filtered the vertical and pressure records to 0.3-0.6 Hz and 0.4-2 Hz respectively to avoid the effects of noise (microseisms, anomalous sensor noise, etc.). We then used an interactive GUI to adaptively adjust the time window (nominally spanning 3 seconds before to 5 seconds after the first break) and filter frequencies to maximize the prominent direct *P*-wave signal in the cross-correlation. We rejected traces based on several criteria including low signal-to-noise ratio (rejected if < 3), anomalous *P*-wave amplitude (rejected if <0.1x or >10x the event mean), and similarity with reference waveform (determined by visual check and cross-correlation coefficient, the latter of which was used to weight the MCCC inversion).

Combining pressure and vertical record travel time measurements:

We tested several approaches for combining these two related single-channel datasets (including simple averaging, simple concatenation, and least squares re-computation across multicomponent pairwise measurements). All approaches produced a travel time dataset that yielded extremely similar tomographic results, so we chose the following combination scheme: If both vertical and pressure measurements were available for a certain event, then only measurements from the channel with more usable traces were retained.

Tomographic model setup

Our differential travel time tomography used a first Fresnel zone paraxial approximation to the Born theoretical kernel (Schmandt & Humphreys, 2010), with updated normalization and voxel-volume terms (Brunsvik et al., 2021), to account for finite frequency sensitivity of travel times to 3-D slowness structure. Finite frequency kernels were constructed by interpolating the ray-normal first Fresnel zone radius at 5 km increments along the ray path. We used 1-D ray tracing through the IASP91 reference model (Kennet & Engdahl, 1991) and accounted for station elevations from multibeam depth soundings (although these elevation corrections have minor effect on the travel times).

The model space comprised a cartesian grid rotated ϕ degrees clockwise from north, with horizontal node spacing of 30 km, extending 300 km in all directions beyond the limits of the OBS array. We tested various values of ϕ for 2-D inversions (see below) obtaining a preferred value of ϕ=25˚ (this value was used for consistency with the gravity and 2.5-D inversions, but the choice of coordinate rotation has almost zero effect on the 3-D inversions). Vertical nodes were spaced every 30-40 km between 40 and 300 km depth, with an additional shallow layer of nodes at 6 km to absorb shallow structure (in addition to the station terms). These depth bounds were chosen to approximately match station spacing (~40 km) and array aperture (~300 km considering station dropouts), respectively.

To regularize the inverse problem we applied both model norm damping and first derivative damping (*i.e.*, "flattening"), minimizing the following cost function:

$$E = \|\mathbf{W}(\mathbf{Gm} - \mathbf{d}_{obs})\|^2 + \gamma\|\nabla\mathbf{m}_0\|^2 + \varepsilon\|\mathbf{m}_0\|^2 + \varepsilon_{evt}\|\mathbf{c}_e\|^2 + \varepsilon_{sta}\|\mathbf{c}_s\|^2$$

Where $\mathbf{G} = [\mathbf{G}_0\ \mathbf{G}_e\ \mathbf{G}_s]$, $\mathbf{m} = \begin{bmatrix}\mathbf{m}_0\\ \mathbf{c}_e\\ \mathbf{c}_s\end{bmatrix}$. In these expressions, $\mathbf{m}_0$ is the vector of fractional perturbations to the initial slowness model, $\mathbf{c}_\mathrm{e}$ is the N_{evts}-length vector of event static times, $\mathbf{c}_s$ is the N_{stas}- length vector of station static times, $\mathbf{d}_{obs}$ is the N_{obs}-length vector of differential travel times, and $\mathbf{G}_0$ is the data kernel matrix with $[G_0]_{ij} = \partial d_i/\partial[m_0]_j$, $\mathbf{G}_e$ is the matrix with $[G_e]_{ik} = \delta_{e(i),k}$ (where $e(i)$ represents the index of the event corresponding to i_{th} seismic ray), $\mathbf{G}_s$ is the matrix with $[G_s]_{il} = \delta_{s(i),l}$ (where $s(i)$ represents the index of the receiver station corresponding to i_{th} seismic ray), $\mathbf{W}$ is a N_{obs}-square diagonal matrix of data weights proportional to the inverse of the standard deviations (σ_d) estimated *a posteriori* during MCCC process. Since estimated differential travel time uncertainty is sometimes unreasonably small, we set a minimum standard deviation of 0.625s, equal to 1/20 of the central filter period. ∇ is the first derivative operator, γ is the smoothing parameter, ε is the damping parameter, and ε_{evt}, ε_{sta} are the damping parameters for event and station static times. Optimal regularization parameter values were determined by L-test (see below), and we fixed ε_{evt} and ε_{sta} to be 0.01 and 5 respectively. Finally, in order to avoid edge effects, damping in the shallowest (≤40 km) and deepest (300 km) layers was increased by a factor of 1.5 compared to the rest of the model volume. For our preferred model, the final RMS error was 0.23s, the RMS of $\mathbf{c}_e$ values was 0.10 s and the RMS of $\boldsymbol{c}_s$ values was 0.01 s.

We used the weighted variance reduction as another measure of the goodness of data fit, computed as $wvr = 100\left(1 - \frac{var(\mathbf{W}[\mathbf{Gm}-\mathbf{d}_{obs}])}{var(\mathbf{Wd}_{obs})}\right)$, where $var()$ is the variance operator. Hypothetically, perfectly fit data would have a wvr =100% (in practice this is impossible, due to irreducible date noise) and wholly un-fit data would have a wvr = 0%, or <0% if the (spurious) model actually worsens the data fit.

Optimizing Tomographic Regularization choices

The regularization was designed to balance data fit, model norm, and model roughness. To achieve this, we used an L-test to search for optimal values of ε and γ, grid searching in the range

0-10 for both parameters. We introduced the term "X", capturing the combination of normalized model norm and roughness:

$$X = \left(\frac{1}{3}\right)\frac{||\boldsymbol{m}||_2}{max\left(||\boldsymbol{m}||_2\right)} + \left(\frac{2}{3}\right)\frac{||\boldsymbol{\nabla m}||_2}{max\left(||\boldsymbol{\nabla m}||_2\right)}$$

where $||\boldsymbol{x}||_2$ represents the L2 norm, ∇ is the gradient matrix, and the 1:2 weighting was determined *ad hoc* to produce reasonable looking models. We analyzed the trade-off between model roughness and weighted data variance reduction, wvr, (Figure S3) by minimizing the penalty function $P = 100X - wvr$ (where the factor of 100 normalizes both terms to the range 0-100). These tests yielded preferred regularization parameters of $\varepsilon = \gamma = 4$ (Figure S3).

Testing the model space: 2.5D inversions, recovery tests, and squeezing tests

"2.5-D" inversions were implemented by zero model variation (through heavy smoothing) along the horizontal direction perpendicular to ϕ. We then grid searched through possible values of ϕ in increments of 5˚, seeking the direction that provided the greatest reduction in data misfit (Fig. 3b and Fig. S7).

For synthetic recovery (input-output) tests, we attempted to fit synthetic data computed by forward propagation through toy models ($\boldsymbol{d}_{test} = \boldsymbol{G}\boldsymbol{m}_{test}$) to which we added Gaussian noise using standard deviations estimated from MCCC measurements.

We used "squeezing tests" to probe the depth range of mantle anomalies required by the data. For these, we conducted a suite of inversions for which the model nodes below a deeper squeezing depth z_d or above shallower squeezing depth z_s, were very heavily damped. This yields a reformatted inversion matrix for the squeezed inverse problem $\boldsymbol{G}'\boldsymbol{m}_1 = \boldsymbol{d}$. $\boldsymbol{G}'$ includes damping that 'squeezes' any structure out of these volumes of the model, and thus forces the inversion to attempt to fit observed data with only a subset of the model nodes. For squeezed inversions, we fixed the event and station static times to values derived from the non-squeezed inversion. To quantitatively compare the squeezed models, we computed two metrics: the weighted variance reduction (wvr) and the L1 norm of $\boldsymbol{m}_2$. $\boldsymbol{m}_2$ is the model obtained through an un-squeezed inversion of $\boldsymbol{G}\boldsymbol{m}_2 = \boldsymbol{r}$ where squeezing is relaxed such that the entire model space is available to fit the data residual $\boldsymbol{r} = \boldsymbol{d} - \boldsymbol{G}'\boldsymbol{m}_1$ from the 'squeezed' inversion. This yields structure that is unable to be captured by the squeezed model but is nevertheless important for fitting the data. Higher values of wvr and lower values of $||\boldsymbol{m}_2||_1$ for a given squeezing test indicate the data more strongly require structure in the un-squeezed layers of that model.

Velocity-temperature calculation

In order to understand the implications of our tomography models for state variables, we forward model mantle velocities. We contrast the predicted seismic velocity for a parcel of “upwelling” mantle at 1350˚C (T_a) with that for a colder parcel of “downwelling” mantle at $T = T_a - \delta T$, where we seek a δT to fit our observations. We use the database of Abers and Hacker (2016) for anharmonic velocities, assuming a pressure of 5 GPa, and a lherzolitic composition. A more depleted (harzburgitic) downwelling mantle would be ~0.02 km/s slower. We account for the effects of anelasticity using the model of Jackson and Faul (2010), assuming a 1 mm equilibrium grainsize (Behn et al., 2009), and an average seismic frequency appropriate to our travel time measurements of 0.5 Hz. With these parameters, a δT = 500˚C yields a V_P contrast of 4.8% between the downwelling (8.29 km/s) and upwelling (7.90 km/s) cells, matching tomographically observed peak to peak variations. Note that using the pre-melting anelasticity model of Yamauchi and Takei (2020) predicts a diminished contrast of 3.6%, due to less strong anelastic velocity reduction at high temperature. In the absence of experiments demonstrating a strong effect on the bulk modulus we assume that anelasticity, and the consequent physical dispersion, affects only the shear modulus. Non-negligible bulk attenuation would serve to exaggerate the velocity contrast. To explore the effect of putative melt, we adjust the anharmonic moduli according to Hammond and Humphreys (2000), and modify the anelasticity calculating by reducing the pre-factor of the diffusion creep timescale (Eilon & Abers, 2017; Holtzman, 2016) to account for the chemical and geometrical (predicted by contiguity theory (Takei & Holtzman, 2009)) effects of melt. As an example, this approach predicts that 0.2% *in situ* melt will reduce shear viscosity by a factor of 6. With these parameters, a δT = 300˚C and 0.5% *in* situ melt in the hotter (upwelling) mantle also yields the observed V_P contrast of 4.8% between the downwelling (8.13 km/s) and upwelling (7.75 km/s) cells.

Admittance, coherence, and gravity correction

We computed the free air admittance and coherence between differential gravity and bathymetry in the 2-D wavenumber domain, averaging over wavenumber annuli of width 0.017km^{-1}. We removed a planar trend from both fields before calculating the spectra. Admittance (Q) in each wavenumber band $(k)$was calculated as the weighted average spectral ratio between the Fourier transformed gravity, $G(k)$, and bathymetry $T(k)$, weighting by the bathymetry:

$$\mathrm{Q} = \frac{\sum_{\mathrm{i}}^{N} \frac{\mathrm{G(k)_i}}{\mathrm{T(k)_i}} |\mathrm{T(k)_i}|}{\sum_{\mathrm{i}}^{\mathrm{N}} |\mathrm{T(k)_i}|}$$

where i is the index among the N Fourier coefficients within the wavenumber band. Since the spectra are complex, we calculate separate admittance spectra for the sine and cosine terms, then average the two. Errors are determined as the standard errors of weighted means. We also calculate the theoretical admittance spectrum accounting for upward continuation and assuming a 7 km-thick crust (z_c), densities of 1030 kg m^{-3}, 2750 kg m^{-3}, and 3300 kg m^{-3} for the water, crust and mantle layers, and an average water depth ($\bar{z}$) of 4600 m:

$$\mathrm{Q_T}(k) = 2\pi\mathrm{G}\{[\rho_c - \rho_w] + [\rho_m - \rho_c]\, exp(-z_c k)\}\, exp(-\bar{z}k)$$

where the non-italicized G represents the gravitational constant. The coherence is calculated as:

$$\gamma^2 = \frac{(\sum_i^N |G(k)_i\, T(k)_i^*|)^2}{(\sum_i^N T(k)_i\, T(k)_i^*)\,(\sum_i^N G(k)_i\, G(k)_i^*)}$$

With standard errors estimated from

$$\Delta\gamma^2 = (1-\gamma^2)(2\gamma^2/N)^{1/2}$$

Finally, we calculated the mantle Bouguer anomaly (MBA) by subtracting the effect of bathymetry in the spectral domain using the theoretical admittance (*i.e.*, agnostic of any true compensation; assuming constant thickness crust). Since our bathymetry coverage at long and short wavelengths is uneven, we also apply a 400-20 km cosine bandpass filter to the MBA.

Gravity modelling

We predicted 1-D gravity variations at the top of a 2.5-D dV_p tomography model as follows: We converted from velocity to temperature assuming $\frac{dT}{dV_p}$ = 54 K/%. This conservative value implicitly assumes that melt modifies velocities but has no substantial effect on density. We converted from temperature variations to density anomalies using a fixed (*i.e.*, not depth dependent) thermal expansion coefficient of 3.5e-5, and a reference density of 3250 kg/m^3. To avoid edge effects in the gravity modelling, at each depth we decomposed 1-D density variation into a series of sines and cosines with log-spaced wavelengths from 60-360 km. We used the simple relationship for upward continuation of sinusoidal vertical gravity perturbations: $\Delta g_Z(x) = 2\pi G\; dh\; \delta\rho \sin\left(\frac{2\pi x}{\lambda}\right) \exp\left(-\frac{2\pi z}{\lambda}\right)$, where G is the gravitational constant, z is layer depth and dh is layer thickness, $\delta\rho$ is density perturbation (the coefficient of the sinusoid), and λ is the wavelength of the anomaly. Cosine variations are handled analogously.

Supporting information figures

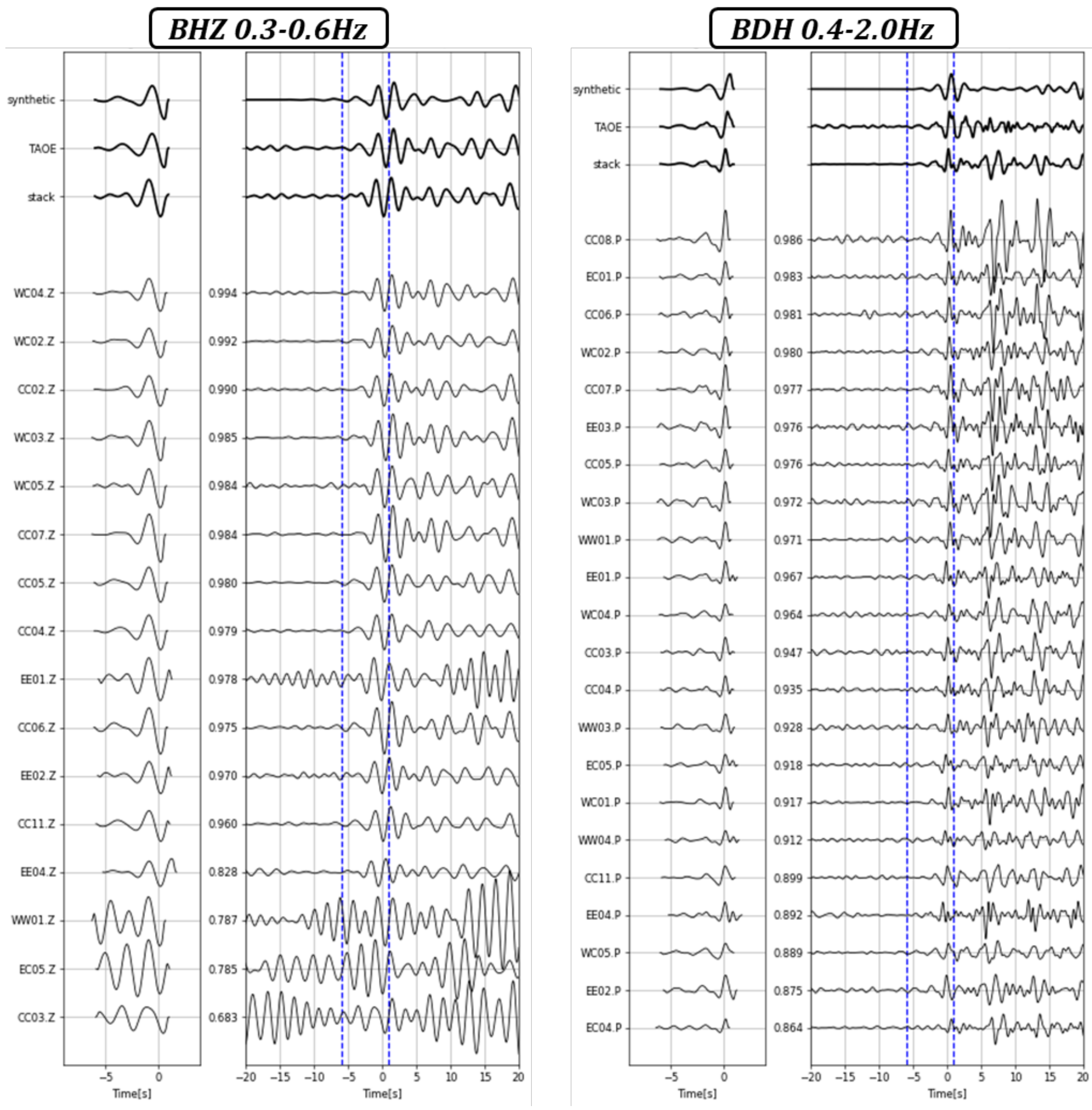

Figure S1. *MCCC differential travel time measurement example for event 2018-11-30 17:29 (Mw7.1) showing vertical channel (BHZ) and pressure channel (BDH). The distinct filter bands for the two components are given at top. For each component, the left column shows post-alignment trace segments for cross-correlation and the right column shows pre-alignment traces with the hand-selected time window indicated by blue lines. The cross-correlation coefficient between each individual trace and the stack (for that component) is given between the columns. At top, the stack of the traces (after alignment) is compared to the synthetic trace from Syngine* (Incorporated Research Institutions for Seismology, 2015)*, as well as a vertical seismic record from ~600km away land station TAOE. Note that the polarity of synthetic and TAOE waveform is flipped for comparison to the pressure channel waveform.*

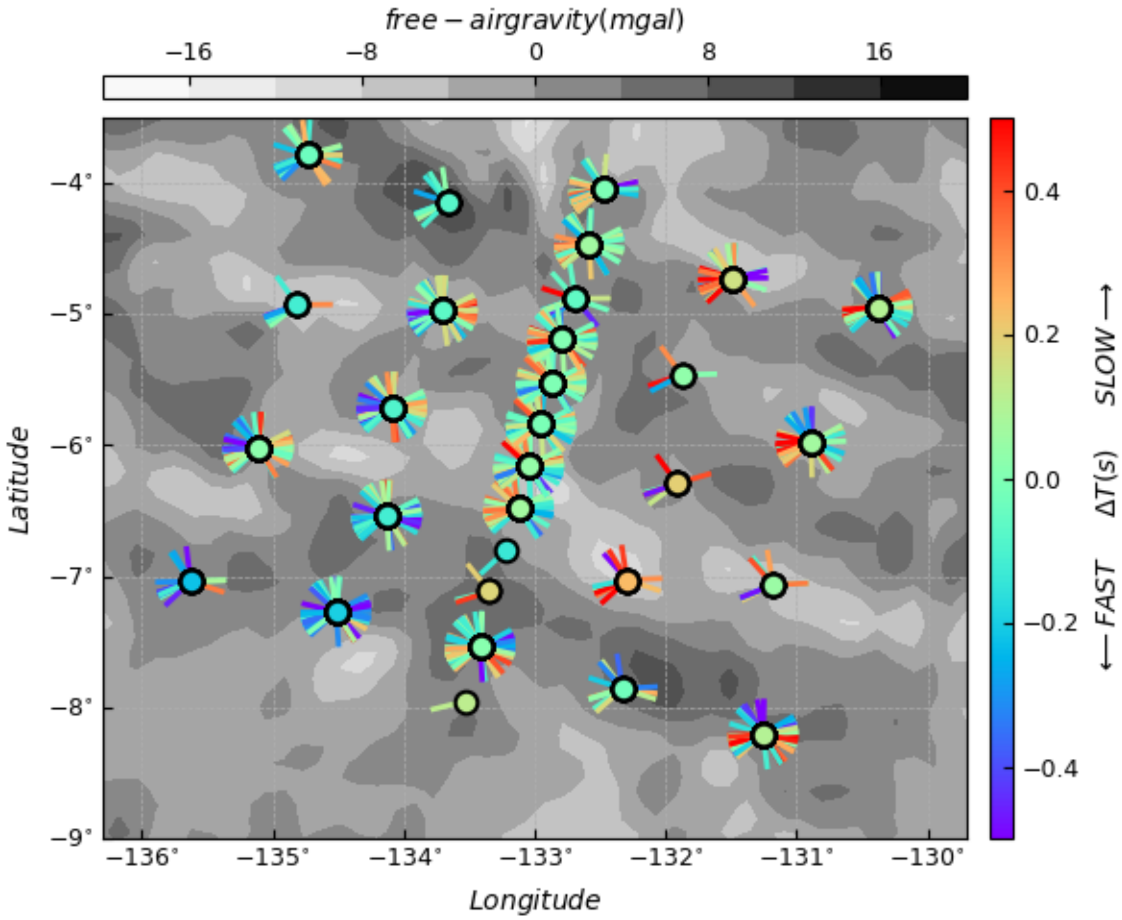

Figure S2. *P-wave differential travel time measurements. Compilation of measurements on both BHZ and BDH components, where each spoke is one measurement, coloured by relative arrival time and pointing in the station-event azimuth. Circles at the station locations indicate mean relative arrival times. The background greyscale map shows free air gravity anomalies.*

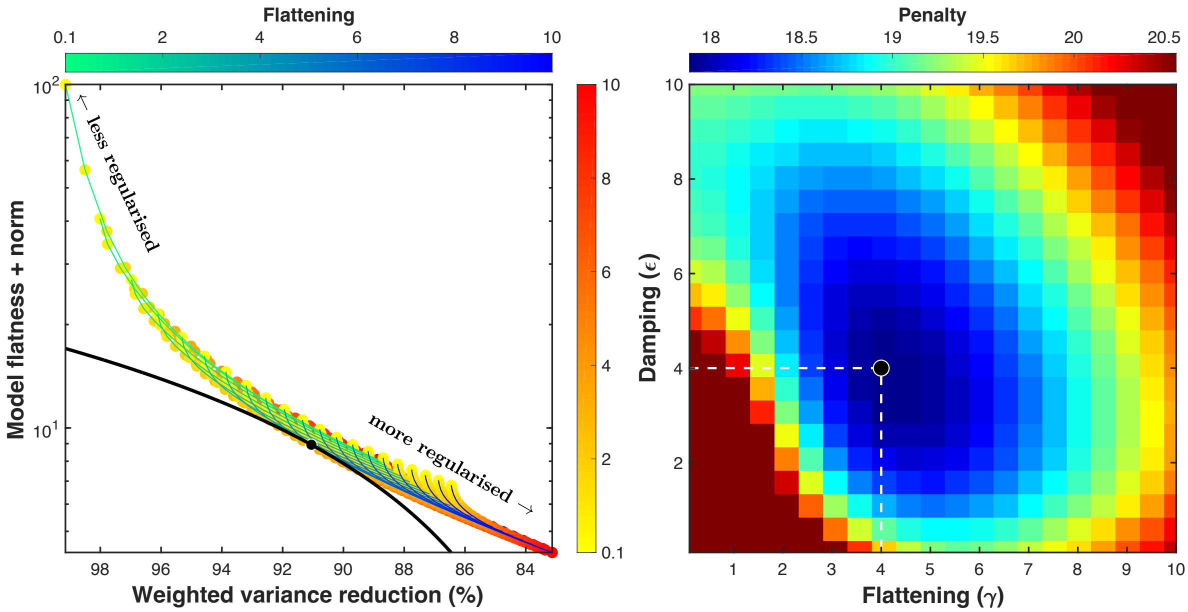

Figure S3. *Tests for optimal regularization parameters used for the inversion. Results of grid-searching for preferred weights of model norm damping (epsilon) and first-derivative damping ("flattening"; gamma) used in the weighted least squares objective function.* ***Left:*** *Trade-off between variance reduction (a measure of data fit) and model norm/roughness (computed as the sum of the norms of the model values and the first derivative values). Each dot represents a single inversion, where dot colour indicates damping weight, and line colour indicates flattening weight. Black dot indicates the preferred value from (b) and black line shows the contour of equal penalty value associated with this point.* ***Right:*** *Contour plot of penalty function computed from a weighted sum of misfit and model norm/roughness, with weighting chosen empirically. Minimum value and associated regularization weights (ε = 4, γ = 4) shown.*

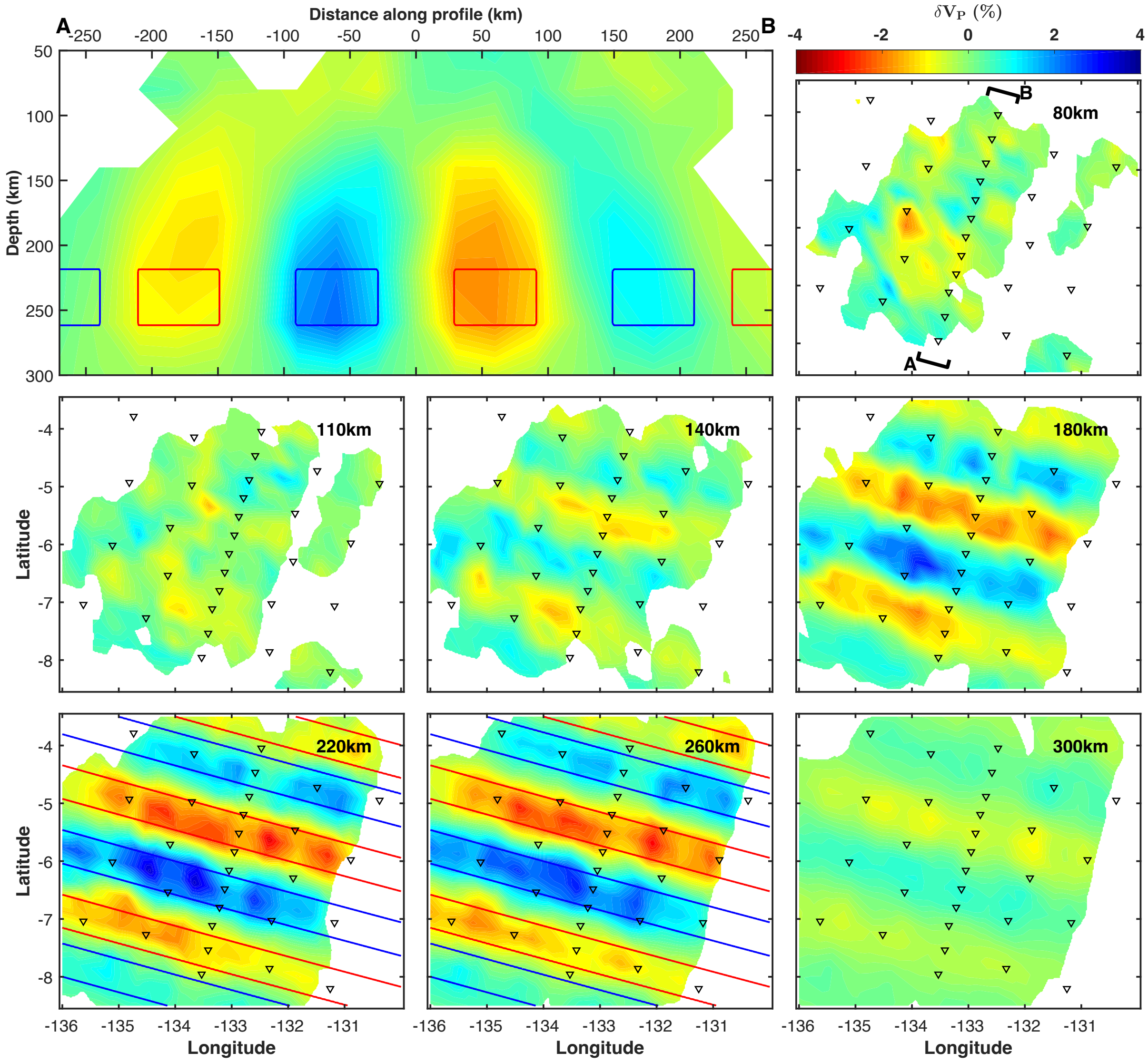

Figure S4. *Cylindrical rolls synthetic recovery test. Input-output test with buried 2.5-D bodies of alternating velocity. Outline of ±4% input structure shown by red (slow) and blue (fast) lines, superimposed on output tomographic model that uses the same regularization parameters as the true tomography. Regions of the output model with low hit quality are masked out.*

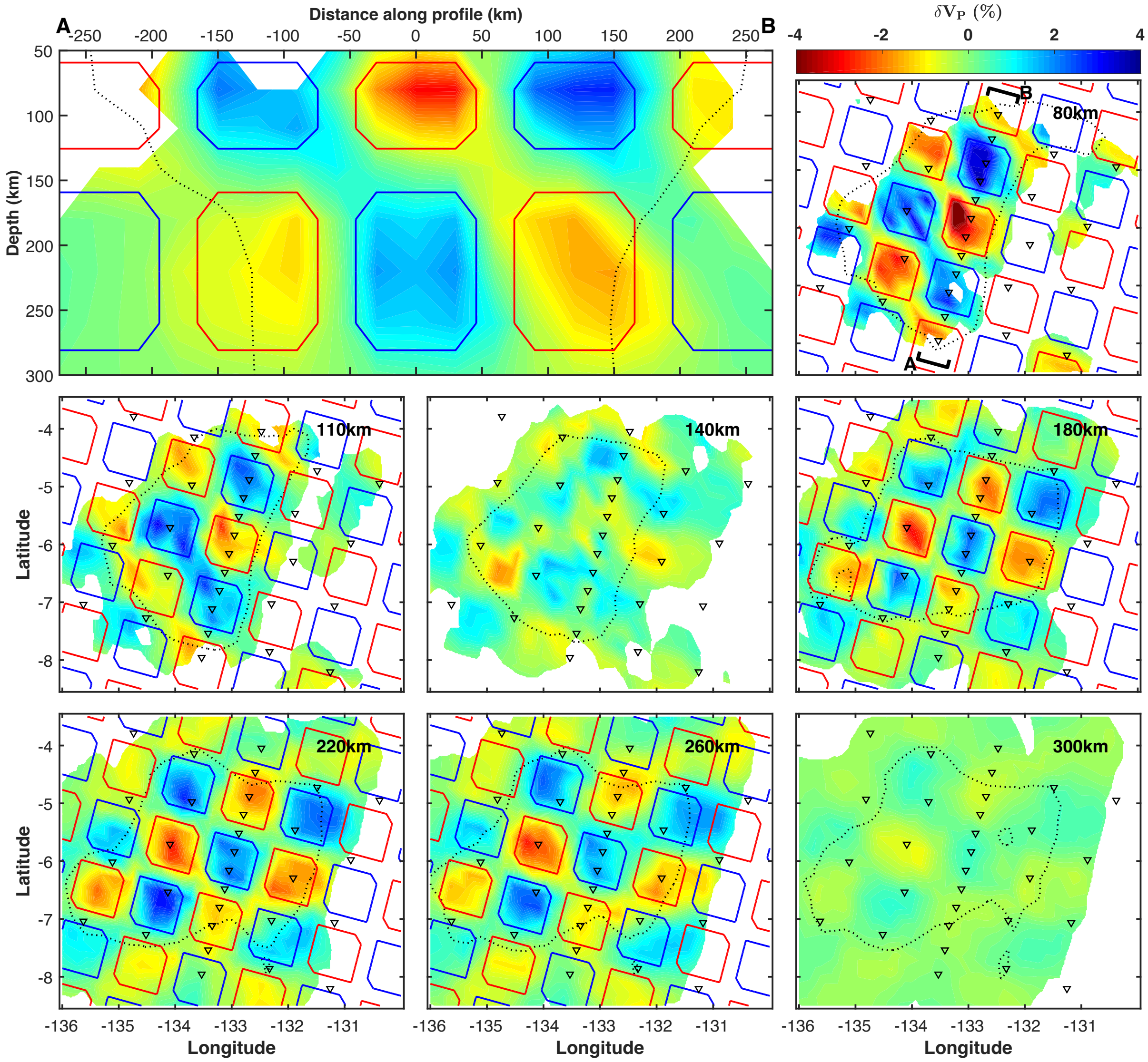

Figure S5. *Checkerboard synthetic recovery test. As for Fig. S4, but for ±4% checkerboard input structure. Semblance, a metric of spatially averaged recovery fidelity* (Zelt, 1998) *was calculated for this model using a spatial length scale equal to the checker size. The 70% semblance contour is shown by the dotted black line; this demarcates the region of very good synthetic model recovery.*

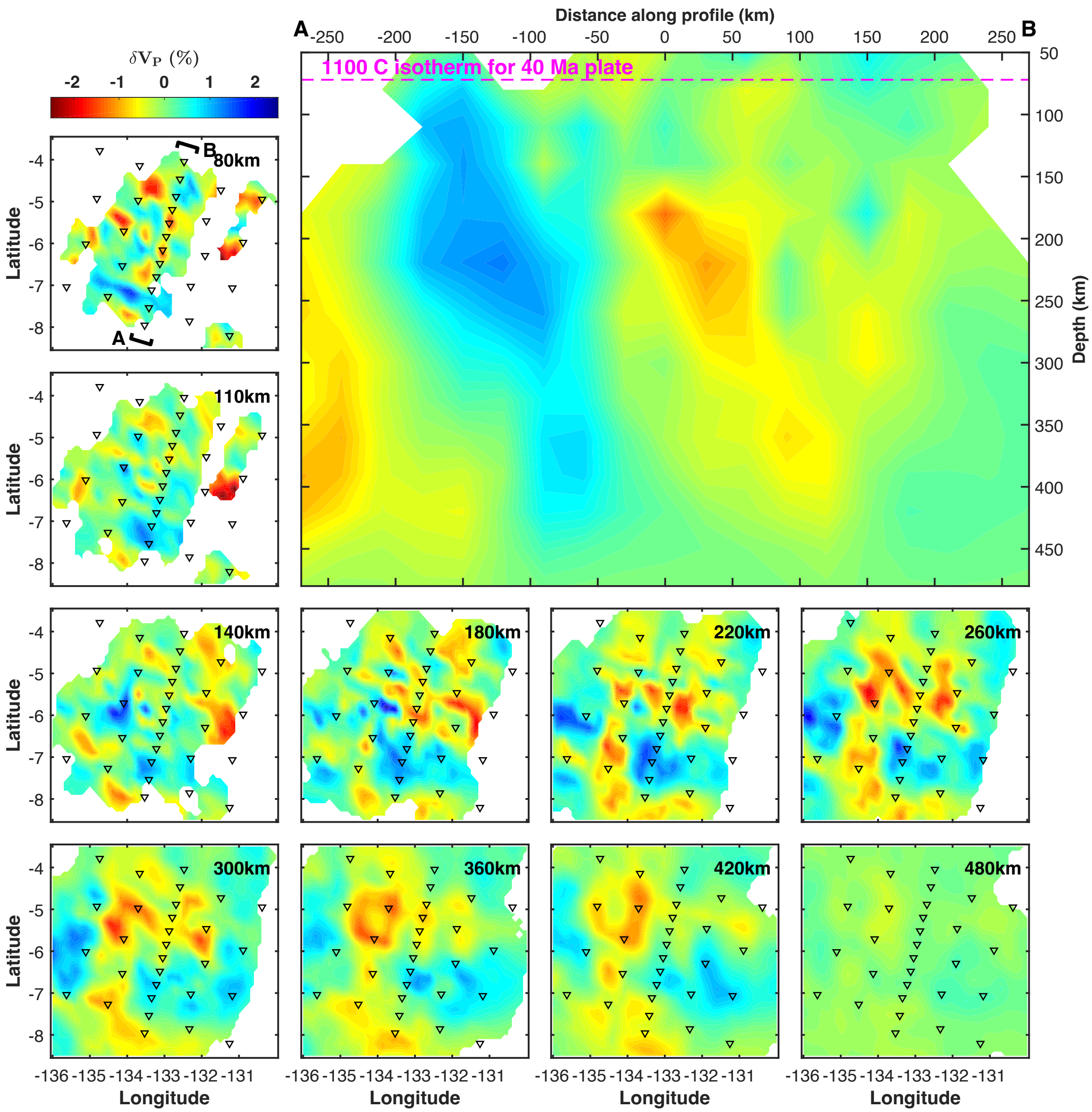

Figure S6. *Inversion with deeper base. This model was obtained by extending the bottom of the model domain to 480km depth. Although there is some smearing of features below the base of the preferred model (300 km), the majority of the structure remains in the 200-300 km depth range and the pattern of the anomalies is essentially unchanged. The weighted variance reduction for this inversion is 87%, compared to 85% for the preferred model.*

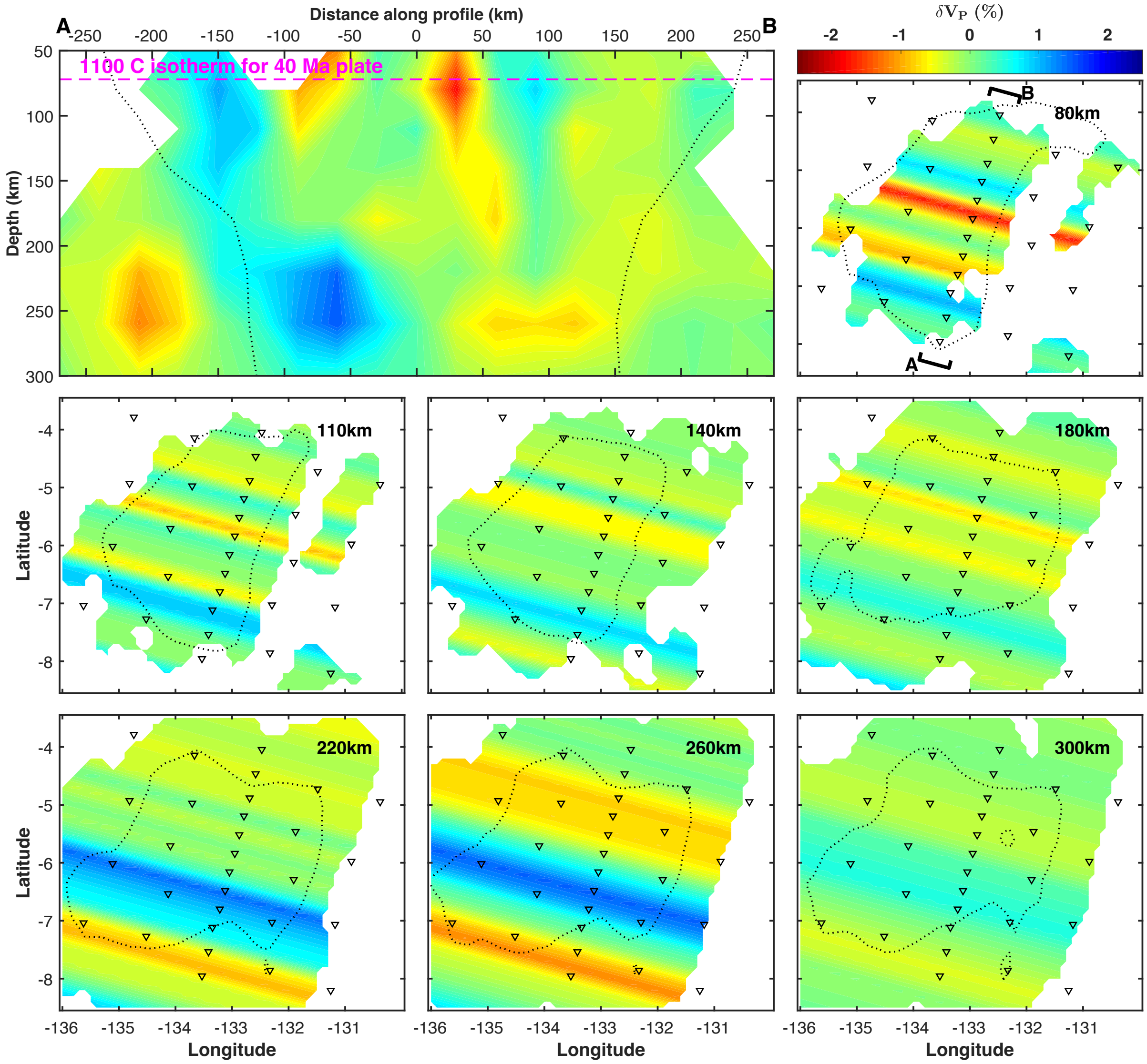

Figure S7. *2.5D data inversion. Similar to Fig. 2, but showing the model inverted with infinite smoothing in the 115˚ direction (i.e., restricting structure to vary in just two dimensions). The weighted variance reduction for this inversion is 63%, compared to 85% for the full 3D model.*

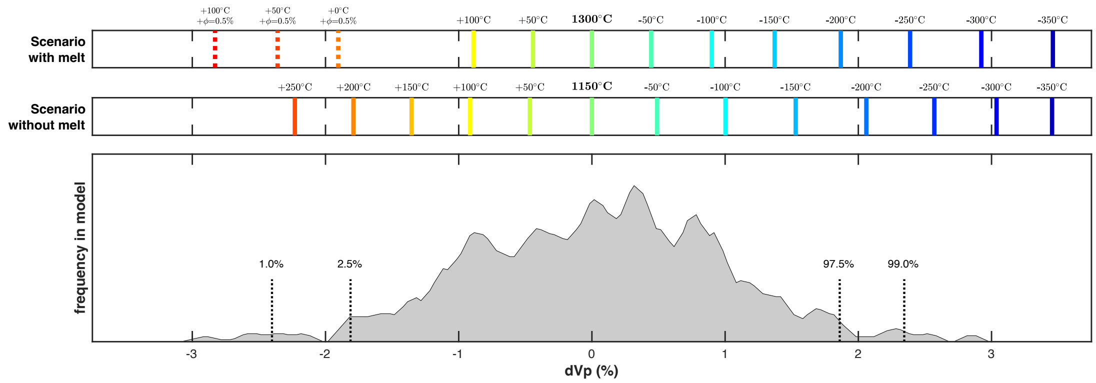

Figure S8. *Illustrative scenarios to explain observed velocity contrast. Bottom panel shows a histogram of node dVp values in the best resolved region of the model (nodes with hit-quality ≥0.3 between 120 and 280km depth, inclusive). 1%, 2.5%, 97.5% and 99% percentile dVp values are indicated. Upper panels show two scenarios for variations in dVp as a function of temperature and melt. Since the observed values provide no absolute velocity constraints, these scenarios are comparably consistent with the observations, despite having different "reference" temperatures (i.e., temperatures corresponding to the mean velocity observed). Velocities are calculated as described in the Text S1. All values shown include the effects of anelasticity, and only the dashed lines include the effects of melt (which modifies moduli both elastically and anelastically).*

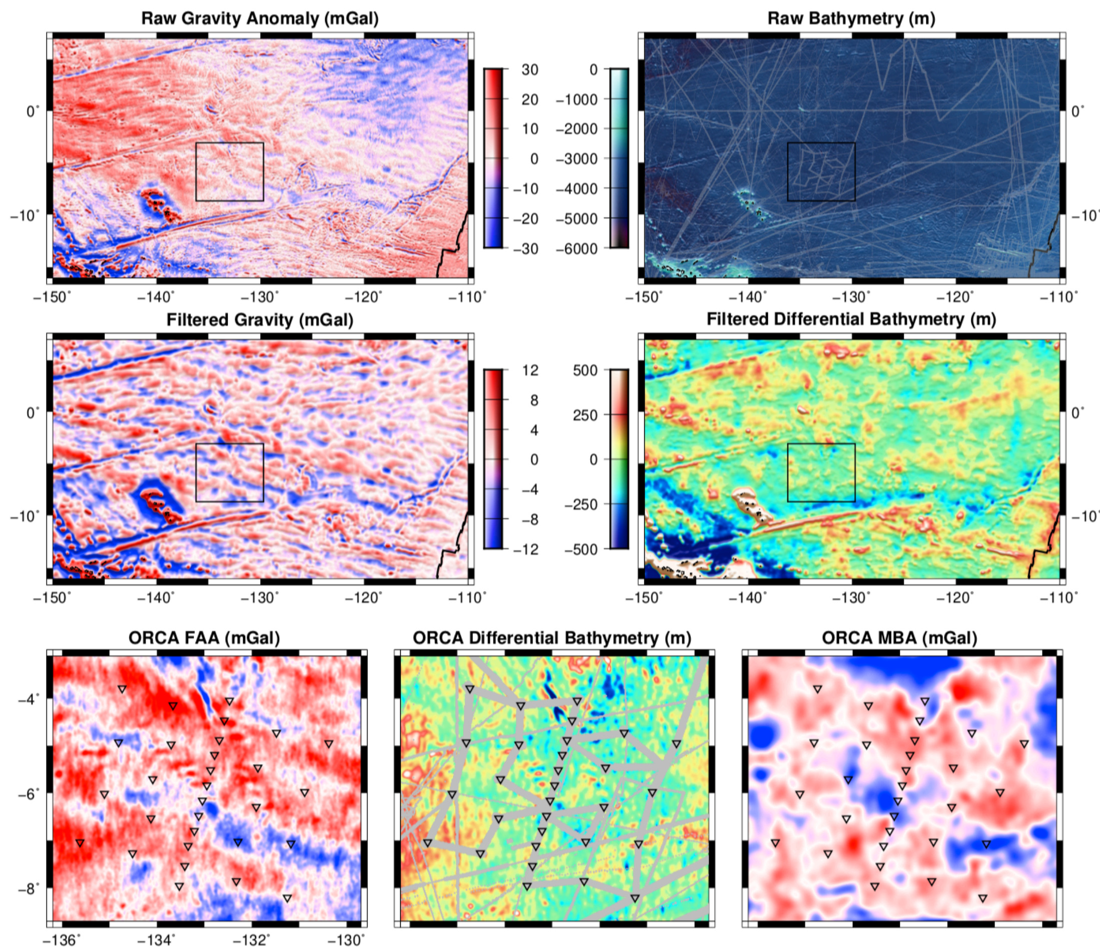

Figure S9. *Residual gravity and bathymetry. Top left: raw free air gravity anomaly [accessed at https://topex.ucsd.edu/pub/global_grav_1min/ on 11/5/21] from satellite altimetry* (Garcia et al., 2014). *Top right: bathymetry from satellite altimetry and ship soundings* (Smith & Sandwell, 1997) *[accessed at https://topex.ucsd.edu/pub/global_topo_1min on 10/14/2021]. Middle left: gravity anomaly as above but filtered in the spatial domain using a 80 km gaussian convolution filter and then a 10^6-10^1 m gaussian bandpass filter, to avoid spectral ringing. Middle right: bathymetry de-meaned and filtered identically to the gravity field. Black box in top two rows shows region in bottom row. Bottom left: Zoomed-in free air gravity anomaly (unfiltered) in the region of our OBS array (black triangles). Bottom center: Zoomed-in de-meaned (but unfiltered) bathymetry, with ship soundings shown. Bottom right: Mantle Bouguer anomaly (see Text S1) filtered from 600-10 km wavelength.*

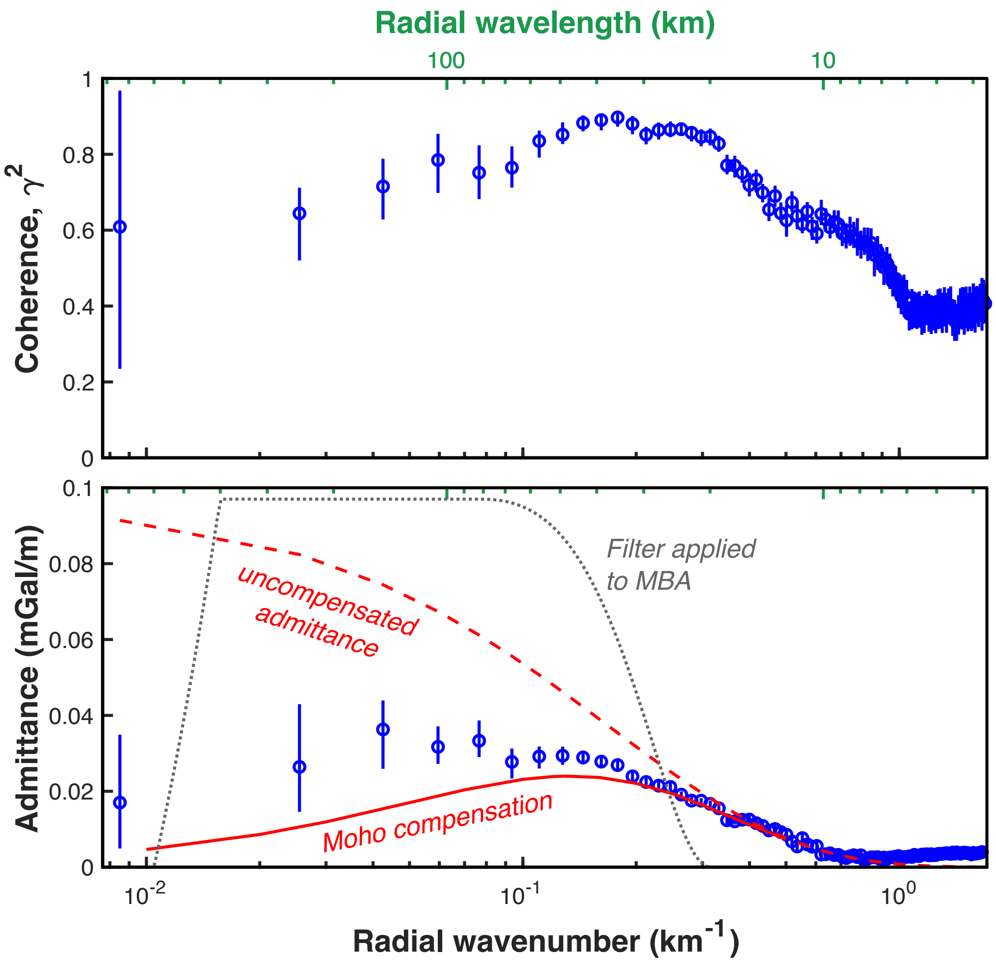

Figure S10. *Coherence and admittance in our study area. Top: Coherence between 2-D free air gravity and bathymetry, with uncertainty calculated using the approach of Bechtel et al.* (1987). *Spectra are averaged across wavenumber annuli with width 0.017 km^{-1}. Bottom: Observed (blue) and predicted (red dashed) un-compensated free air admittance values for uncompensated topography. The former are shown with 10-90th percentile ranges from bootstrap analysis (see Text S1), the latter include the effects of upward continuation and both water-crust and crust-mantle periodic density variations, assuming crustal density of 2750 kg m^{-3}, mantle density of 3300 kg m^{-3}, a constant 7 km thick crust, and average water depth of 4600 m. Solid red line is predicted admittance for topography compensated at the Moho.*